





Solitary Alfvén Waves

ZESSEN HUANG ¹, MARCO VELLI ¹, CHEN SHI ², AND YULIANG DING ¹

¹*Department of Earth, Planetary, and Space Sciences, University of California, Los Angeles*

²*Department of Physics, Auburn University*

ABSTRACT

We present a three-dimensional numerical model of a solitary spherically polarized Alfvén wave packet — an *Alfvénon*, characterized by open field-line topology and magnetic field reversals, resembling the switchbacks observed by Parker Solar Probe to be a nearly ubiquitous feature of turbulence in the inner heliosphere. Direct magnetohydrodynamic simulations of the constructed Alfvénon demonstrates remarkable stability, confirming its nature as an exact, nonlinear solution of the ideal MHD equations.

Keywords: Alfvén Waves (23), Magnetohydrodynamics (1964), Magnetohydrodynamical simulations (1966), Solar wind (1534), Space plasmas (1544)

1. INTRODUCTION

Since the introduction of Alfvén waves in 1942 (H. Alfvén 1942), these fundamental magnetohydrodynamic (MHD) oscillations have been invoked to explain a wide range of phenomena in astrophysical (C. F. McKee & E. G. Zweibel 1995), space (J. W. Belcher & L. Davis 1971; J. Coleman 1968; T. W. J. Unti & M. Neugebauer 1968), and laboratory plasmas (W. Geikelman et al. 1997). Recent observations from the Parker Solar Probe (PSP) (N. J. Fox et al. 2016; N. E. Raouafi et al. 2023) reveal that the pristine solar wind in the upper corona (J. C. Kasper et al. 2021) is permeated by large-amplitude magnetic field fluctuations termed “switchbacks”. Typically, these fluctuations are solitary, large-amplitude magnetic field reversals with quasi-constant field magnitude, accompanied by anti-sunward proton jets that exhibit near-perfect Alfvénic correlation (S. D. Bale et al. 2019). They also display field-aligned electron strahls with the same pitch-angle both inside and outside the reversal regions, suggesting topologically open folds of the magnetic field lines (J. C. Kasper et al. 2019). Consequently, a substantial portion of switchbacks are spherically polarized Alfvén waves (SPAWs)—exact nonlinear solutions of the ideal MHD equations (M. L. Goldstein et al. 1974; A. Barnes 1981).

Figure 1 shows a typical interval from the perihelion of PSP’s 19th encounter at $11.75 R_{\odot}$ (S. D. Bale et al. 2016; J. C. Kasper et al. 2016). Panels (a), (g), and (h) demonstrate that this interval captures a single stream of highly magnetized (plasma $\beta \ll 1$) pristine solar wind with quasi-constant $|B|$ and proton density n_p (proxied

with electron number density from Quasi-Thermal-Noise O. Kruparova et al. (2023)). Panel (b) clearly reveals one-sided solitary magnetic perturbations superposed on the otherwise sunward *unperturbed* coronal magnetic field—a feature also observed near 1AU (J. T. Gosling et al. 2009). Around 6:35, 6:37, and 6:55, three well-separated switchback packets are evident. Panels (d–f) show \vec{b} (left axis, \vec{B} converted to velocity units using $\langle n_p \rangle$) and \vec{u} (right axis) on matched scales (averages are subtracted for t and n components), revealing impeccable Alfvénic correlation within the measurement uncertainties of \vec{u} . Notably, the local Alfvén speed V_A exceeds the unperturbed baseline u_r , indicating that PSP is inside the solar corona (J. C. Kasper et al. 2021). The electron pitch angle distribution in panel (c) shows clear field-aligned anti-sunward electron strahls both inside and outside the switchbacks, confirming open field-line topology.

Several studies have attempted to construct (solitary) SPAWs. For instance, A. Tenerani et al. (2020) and C. Shi et al. (2024b) developed 2.5D models of switchbacks (2D coordinates, 3D vector fields), while M. Shoda et al. (2021) and J. Squire & A. Mallet (2022) constructed 3D turbulent divergence-free vector fields with quasi-constant magnitude. However, the models from A. Tenerani et al. (2020) and C. Shi et al. (2024b) necessarily contain topologically closed regions (as demonstrated in Appendix A, 2.5D solitary solutions must contain topologically closed regions), whereas the switchbacks produced by (M. Shoda et al. 2021; J. Squire & A. Mallet 2022) lack spatial isolation. As noted by J. Squire & A. Mallet (2022), the primary challenge in modeling

SPAWs lies in constructing a divergence-free unit vector field. Building on this insight, we develop a convergent algorithm (hereafter, the algorithm) to construct a numerical model of an open field-line, solitary, three-dimensional SPAW packet—an Alfvénon.

The remainder of this paper is organized as follows. Section 2 outlines the solitary Alfvén waves solution from ideal MHD equations. Section 3 describes the algorithm and the Alfvénon model. Section 4 presents results from direct MHD simulations of the constructed Alfvénon. Finally, Section 5 discusses the simulation results, the nomenclature of Alfvénon, and concludes the study.

2. SOLITARY ALFVÉN WAVES

We begin from the ideal MHD equations:

$$\frac{\partial \rho}{\partial t} + \nabla \cdot (\rho \vec{u}) = 0, \quad (1)$$

$$\rho \left[\frac{\partial \vec{u}}{\partial t} + (\vec{u} \cdot \nabla) \vec{u} \right] = -\nabla \left(p + \frac{B^2}{2\mu_0} \right) + \frac{1}{\mu_0} (\vec{B} \cdot \nabla) \vec{B}, \quad (2)$$

$$\frac{\partial \vec{B}}{\partial t} = \nabla \times (\vec{u} \times \vec{B}), \quad (3)$$

$$p\rho^{-\gamma} = \text{const}, \quad (4)$$

$$\nabla \cdot \vec{B} = 0, \quad (5)$$

where ρ is the plasma density, \vec{u} is the flow velocity, p is the pressure, \vec{B} is the magnetic field, γ is the adiabatic index, and μ_0 is the vacuum permeability. To proceed, we impose three assumptions inspired by observations: (A1) constant $|\vec{B}|$; (A2) constant ρ ; (A3) constant p . Under these assumptions, we look for *solitary Alfvénic* solution of $\vec{B}(\vec{r}, t)$ and $\vec{u}(\vec{r}, t)$.

First, we make the conversion: $\vec{b} = \vec{B}/\sqrt{\mu_0\rho}$. (A1–A3) guarantee $\nabla \cdot \vec{u} = 0$ and $\nabla \cdot \vec{b} = 0$. Consequently, Eqs. (2)–(3) reduce to:

$$\frac{\partial \vec{u}}{\partial t} = (\vec{b} \cdot \nabla) \vec{b} - (\vec{u} \cdot \nabla) \vec{u}, \quad (6)$$

$$\frac{\partial \vec{b}}{\partial t} = (\vec{b} \cdot \nabla) \vec{u} - (\vec{u} \cdot \nabla) \vec{b}. \quad (7)$$

The ∇ operator only acts on spatially dependent part of \vec{b} and \vec{u} , and hence we can decompose \vec{b} into unperturbed and perturbative parts: $\vec{b} = \vec{b}_0 + \vec{b}_1(\vec{r}, t)$. *Solitary* solution dictates $\vec{b}_0 = \vec{b}(\infty)$, and thus $|\vec{b}| = |\vec{b}_0| = |\vec{b}_0 + \vec{b}_1|$, i.e. \vec{b}_1 is restricted on a constant sphere *defined* by \vec{b}_0 , illustrated in Fig. 2. Similarly, we decompose \vec{u} into $\vec{u}_0 + \vec{u}_1$. *Alfvénic* solution dictates: $\vec{u}_1 = \pm \vec{b}_1$. Because \vec{b} is Galilean invariant, without loss of generality, we can transform into a frame where $\vec{u}_0 = 0$. In this frame,

Eqs. (6)–(7) reduce to:

$$\frac{\partial \vec{u}_1}{\partial t} = \vec{b}_0 \cdot \nabla \vec{b}_1, \quad (8)$$

$$\frac{\partial \vec{b}_1}{\partial t} = \vec{b}_0 \cdot \nabla \vec{u}_1, \quad (9)$$

where $\vec{b}_0 = \vec{B}_0/\sqrt{\mu_0\rho}$ represents the local Alfvén phase velocity. These yield the wave equations of SPAWs, first derived by (M. L. Goldstein et al. 1974):

$$\frac{\partial^2 \vec{u}_1}{\partial t^2} = (\vec{b}_0 \cdot \nabla)^2 \vec{u}_1, \quad (10)$$

$$\frac{\partial^2 \vec{b}_1}{\partial t^2} = (\vec{b}_0 \cdot \nabla)^2 \vec{b}_1. \quad (11)$$

An important consequence follows from Eqs. (8)–(9). Assuming $\vec{b}_0 = b_0 \hat{x}$ and $\vec{b}_1 = -\vec{u}_1$, Eq. (8) becomes

$$\left(\frac{\partial}{\partial t} + b_0 \frac{\partial}{\partial x} \right) \vec{b}_1 = 0, \quad (12)$$

describing a forward-propagating ($+\hat{x}$) wave $\vec{b}_1(x - b_0 t)$. Similarly, when $\vec{b}_0 = -b_0 \hat{x}$, forward propagation requires $\vec{b}_1 = \vec{u}_1$. Thus for forward-propagating waves, u_{1x} is always positive irrespective of the sign of \vec{b}_0 (Fig. 2). This explains the one-sided anti-sunward proton jets associated with the magnetic switchbacks in the solar wind (J. T. Gosling et al. 2009; S. D. Bale et al. 2019; J. C. Kasper et al. 2019).

Although Eqs. (10)–(11) resemble classical shear or circularly polarized Alfvén wave equations, three crucial distinctions arise: (1) \vec{b}_1 is *solitary*. The original dispersion relation of shear Alfvén waves (H. Alfvén 1942) is derived in Fourier space, implying spatially periodic solutions. (2) \vec{b}_0 is the *unperturbed* field. Consequently, $\vec{b}_0 \neq \langle \vec{b} \rangle$ and $\langle \vec{b}_1 \rangle \neq 0$ over the support of the solitary solution, meaning that the perturbative \vec{b}_1 is *one-sided* (J. T. Gosling et al. 2009), contradicting the averaging approach used in most of the observational studies. (3) \vec{b}_1 is *intrinsically nonlinear*. If both \vec{b}_1 and \vec{b}'_1 are solutions satisfying the constant- $|\vec{b}|$ constraint, their sum $\vec{b}_1 + \vec{b}'_1$ generally violates that constraint, so linear superposition does not hold, contravening the usual Fourier decomposition used in Alfvénic turbulence.

Finally, $\vec{b}_1(\vec{r}, t)$ represents a *perturbation* to \vec{b}_0 . According to Alfvén’s theorem, \vec{b} remains *topologically* unchanged relative to \vec{b}_0 . Therefore, analogous to shear Alfvén waves, solitary Alfvén waves (Alfvénons) should consist of non-trivial twisting of magnetic field lines while preserving field-line density (constant $|b|$).

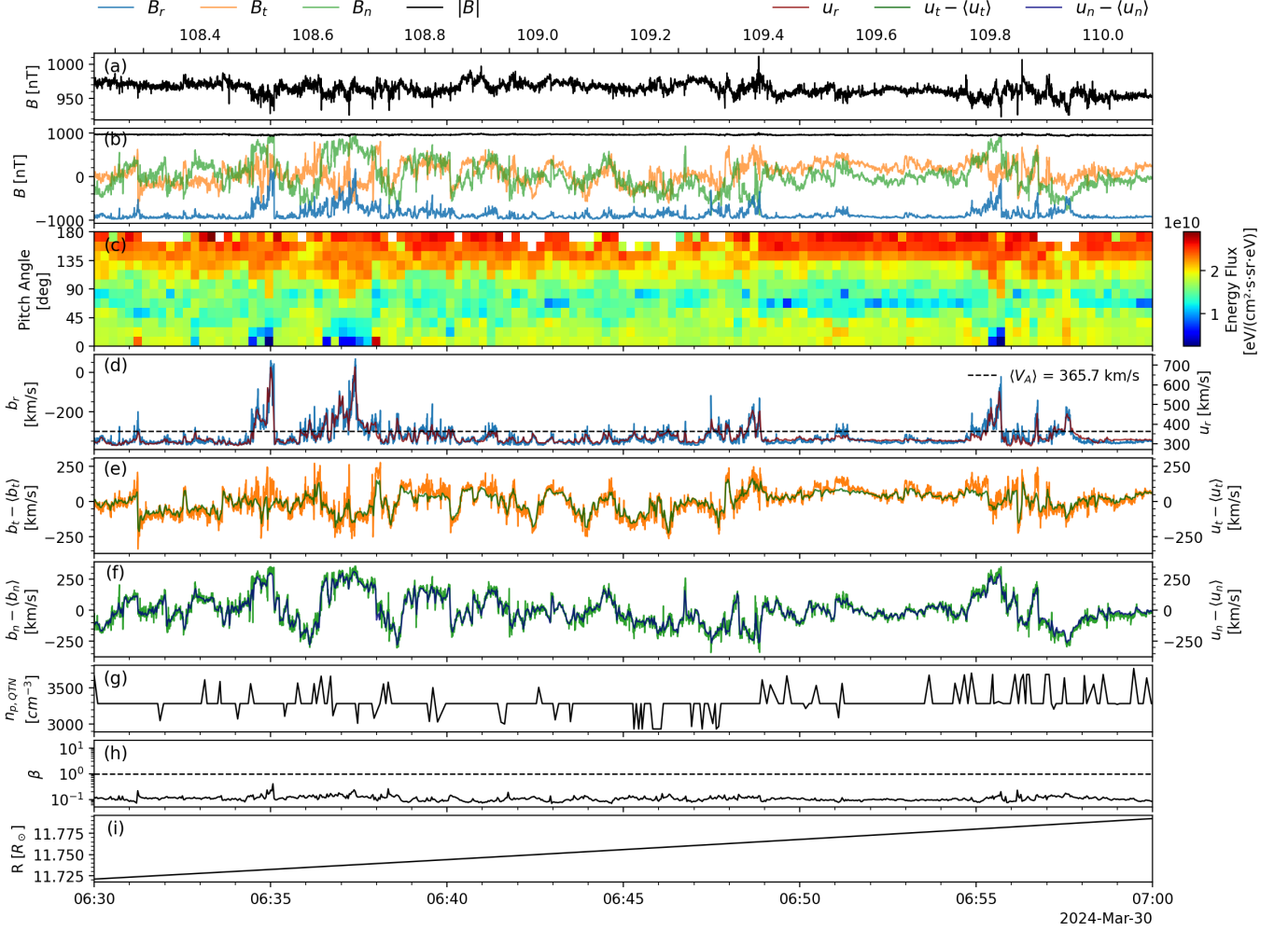


Figure 1. Solitary spherically polarized Alfvén wave packets (switchbacks) from PSP Observations. Panels show (a,b) magnetic field magnitude and components, (c) Electron pitch angle distribution (d-f) velocity-magnetic field correlations (darker lines are proton bulk speeds), (g) proton (electron) number density from Quasi-Thermal-Noise, (h) proton plasma $\beta = n_p k_B T_p / (B^2 / 2\mu_0)$ and (i) radial distance of PSP. Carrington longitude is shown on top.

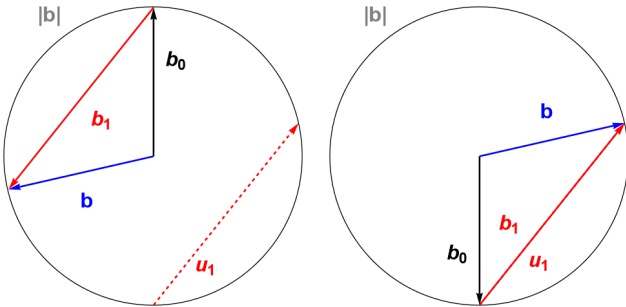


Figure 2. Constant $|B|$ restriction for forward propagating SPAWs. *Left:* forward-pointing \vec{b}_0 . *Right:* backward-pointing \vec{b}_0 .

3. CONSTRUCTING ALFVÉNON

3.1. Convergent Algorithm

The key to create an Alfvénon model is to construct a vector field $\vec{B}(x, y, z)$ that satisfies:

$$\nabla \cdot \vec{B} = 0, \quad |\vec{B}| \simeq 1. \quad (13)$$

Starting from an arbitrary vector field $\vec{F}(x, y, z)$, we invoke the Helmholtz-Hodge decomposition:

$$\vec{F} = \nabla\varphi + \nabla \times \vec{A}. \quad (14)$$

We can remove the divergence by subtracting the gradient of the potential field:

$$\vec{G} = \vec{F} - \nabla\varphi, \quad (15)$$

where φ is solved from the Poisson equation $\nabla^2\varphi = \nabla \cdot \vec{F}$. The resulting field \vec{G} is then normalized pointwise to

unit magnitude:

$$\vec{F}' = \frac{\vec{G}}{|\vec{G}|}. \quad (16)$$

Although this normalization reintroduces a nonzero divergence, repeated application of Eqs. (15) and (16) could drive \vec{G} toward a state that is both divergence-free and of quasi-constant magnitude. Denoting the fields at the n -th iteration by \vec{F}_n and \vec{G}_n , we have:

$$\vec{G}_n = \vec{F}_n - \nabla \varphi_n, \quad (17)$$

$$\vec{F}_{n+1} = \frac{\vec{G}_n}{|\vec{G}_n|}, \quad (18)$$

where $\nabla^2 \varphi_n = \nabla \cdot \vec{F}_n$. Together Eqs. (17) and (18) constitute the convergent algorithm.

3.2. Alfvénon Model

Using the convergent algorithm, we constructed an Alfvénon candidate \vec{G}_A on a 256^3 grid (see Appendix B for algorithm implementation and its convergence.) \vec{G}_A is incredibly complex: It is a quasi-constant unit vector field containing a spatially localized perturbed region. Towards the edges, $\vec{B} \simeq \vec{B}_0 = (1, 0, 0)$. \vec{G}_A remains simply connected—no topologically closed regions exist—field lines enter through the $x = 0$ plane and exit through the $x = 1$ plane (see Appendix D for details.) To visualize \vec{G}_A , we compute the isosurface of:

$$\Phi_B(x, y, z) = |\vec{B}_0 \cdot \nabla \vec{B}|, \quad (19)$$

This quantity is inspired by Eq. (8), where $\vec{b}_0 \cdot \nabla \vec{b}_1$ represents the restoring force for \vec{u}_1 . Assuming constant ρ , the two quantities are equivalent. The isosurfaces are shown in Figure 3.

Φ_B quantifies the local field-line curvature. Figure 3 clearly reveals a perturbed region occupying the center of the domain, with the field remaining uniform outside this region. Two particularly strong perturbed zones appear around $x = 0.35$ and $x = 0.65$. Within both zones, field lines are strongly curved and can even exhibit steep reversals with local $\theta > 140^\circ$, characteristic of magnetic switchbacks. A more detailed investigation of the switchback structure will be addressed in a companion paper. An interactive version of Fig. 3 is available as supplementary material.

Starting from \vec{G}_A , we construct the full numerical model for the Alfvénon to serve as the initial condition for the MHD simulation. Following A2, we set a constant density $\rho = 1$. The most crucial step in constructing a stable Alfvénon is the separation of the perturbations in \vec{B} . The *solitary* nature of \vec{G}_A allows us

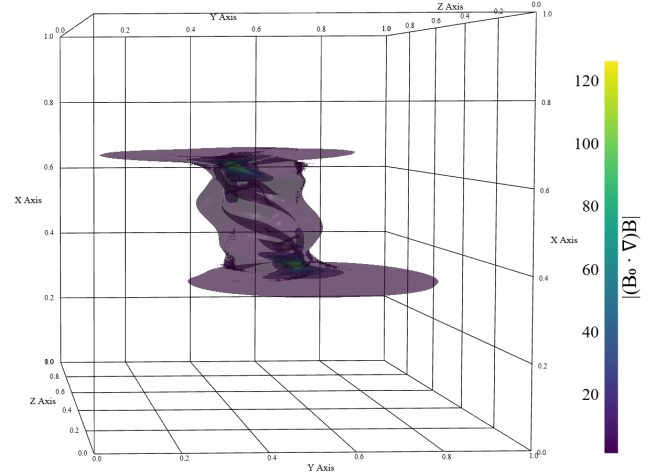


Figure 3. Isosurfaces of $|\vec{B}_0 \cdot \nabla \vec{B}|$.

to determine: $\vec{B}_1 = \vec{B} - \vec{B}_0$. Assuming forward propagation along \vec{B}_0 , we obtain the velocity perturbation as $\vec{u}_1 = -\vec{b}_1 = -\vec{B}_1/\sqrt{\mu_0\rho}$, where we adopt $\mu_0 = 1$. Finally, based on A3, we set a constant pressure $p = 0.1$, yielding a plasma $\beta = 0.2$ that is compatible with typical pristine solar wind conditions (Z. Huang et al. 2024a). We also adopt an adiabatic index $\gamma = 1.1$, which is representative of fast (Alfvénic) solar wind (C. . Shi et al. 2022).

4. MHD SIMULATION

The simulation is conducted with the LAPS code (C. Shi et al. 2024a), which is a pseudo-spectral MHD code assuming *periodic* boundary conditions. In the simulation, the typical time scale is the Alfvén wave passing time $t_A = L_x/b_0$, where $L_x = 1$ and $\vec{b}_0 = \vec{B}_0/\sqrt{\mu_0\rho} = (1, 0, 0)$. Consequently, the wave packet returns to the same location every $t = t_A = 1$, allowing us to recenter the wave packet by shifting the x-axis index based on t .

Figure 4 illustrates the results of the MHD simulation at four different time frames: $t = 0.00$, $t = 0.05$, $t = 5.00$, and $t = 40.00$. We select 2D slices of the simulation box at $ix = 95$, $iy = 151$, and $iz = 118$, which is located within the strongest curved zones depicted in Fig. 3. As shown in (a1), the initial x-profile shows a strong rotational discontinuity at $ix = 95$, resembling typical switchbacks boundaries (e.g. 6:35 and 6:56 in Fig. 1). Panels (a2-4) show the 2D slices of $\theta = \cos^{-1}(B_x/|B|)$, signifying that such significant field line reversals are also present near the chosen point.

Row (b) shows the very first step of the simulation. Comparison of (a1) and (b1) reveals two immediate effects: (1) high- k oscillations are suppressed in all components of \vec{B} and \vec{u} , and (2) the constancy of $|B|$ is violated, particularly at the rotational discontinuity. These

changes arise primarily from the LAPS de-aliasing procedure. The large-amplitude magnetic reversals in \vec{G}_A are spatially sharp, requiring substantial spectral power at high- k modes to maintain both sharp structures and constant $|B|$ on a finite 256^3 grid. Removing these modes via de-aliasing produces localized deviations in $|B|$, as illustrated in Figure 5: at $t = 0.05$, the $|B|$ histogram develops several highly localized outliers. Consequently, magnetic-pressure imbalances seed ρ and p perturbations, rapidly raising σ_ρ (panel a).

Rows (c) and (d) present the profiles at $t = 5.00$ and $t = 40.00$, respectively. The magnitude $|B|$ recovers near-constancy as the physical evolution smooths the initial extremes. Although the switchback amplitude gradually decreases over time, the wave profile remains qualitatively similar to the initial condition through $t = 5.00$, while maintaining near-perfect Alfvénic correlation up to $t = 40.00$. Columns 2–4 further reveal that the wave packet’s spatial structure persists even at $t = 40.00$ despite amplitude reduction, demonstrating notable morphological stability.

As the simulation evolves, σ_ρ initially remains relatively low before growing substantially after $t = 10$. The rapid growth of σ_ρ from $t = 10$ to $t = 30$ indicates parametric decay instability (PDI) seeded by the initial σ_ρ , consistent with previous studies (N. F. Derby 1978; B. D. G. Chandran 2018; A. Tenerani et al. 2020; C. Shi et al. 2024b). The compressive activity heats the plasma at the expense of magnetic energy E_B and kinetic energy E_K , primarily through the term $\nabla \cdot (p\vec{u})$ in the energy equation (C. Shi et al. 2024a) (see Appendix C for diagnostic definitions). Consequently, as shown in Fig. 5 panel (d), the internal energy ΔE_{int} increases while $E_B + E_K$ gradually decreases. Importantly, the simulation employs zero explicit resistivity and viscosity. The excellent conservation of total energy $E_B + E_K + \Delta E_{\text{int}}$ thus confirms that numerical dissipation from de-aliasing remains negligible.

Panel (c) validates the wave packet’s gradual relaxation over time, consistent with the evolution shown in Fig. 4. Panel (d) reveals that the non-Alfvénic energy component steadily increases starting from $t = 20.00$ accompanied with alternating fluctuations of E_B and E_K (residual energy $E_B + E_K + \vec{u} \cdot \vec{b}$), indicating growing presence of persistent sonic modes, likely generated by PDI. Despite this relaxation, the wave packet retains a high degree of Alfvénicity. The observed relaxation likely arises from two mechanisms: (1) wave-wave interactions led by PDI, and (2) phase mixing resulting from small Alfvén speed differences caused by density variations. Notably, the periodic boundary conditions artificially enhance PDI through density perturbations

created by nearby wave packet images, suggesting that the Alfvénon would be substantially more stable under realistic open-field conditions. Future studies should investigate the Alfvénon’s stability across different simulation domains and plasma environments.

In conclusion, the stability and Alfvénicity of the wave packet confirm that the constructed Alfvénon model represents an accurate exact nonlinear solution to the ideal MHD equations.

5. DISCUSSIONS AND CONCLUSIONS

5.1. De-aliasing in the MHD Simulation

The initial imbalances in $|B|$, and consequently in p and ρ , arise primarily from numerical artifacts due to the de-aliasing procedure rather than physical instabilities of the Alfvénon model. In the simulation, we employed de-aliasing option 2 of LAPS, which progressively smooths and damps modes near the Nyquist frequency. Notably, using the same initial conditions with de-aliasing option 1 (classical Orszag 2/3 spherical truncation) produces substantially larger defects in $|B|$, leading to extreme density and pressure voids ($\rho \rightarrow 0$) that cause prohibitively small time steps and halt the simulation. This highlights the subtleties of de-aliasing processes. We have also constructed a smaller-amplitude Alfvénon model with weaker discontinuities; in that case, the de-aliasing-induced imbalances are substantially reduced.

5.2. Why Alfvénon?

Conservation of adiabatic invariant (also called wave action or wave quanta) in the Wentzel–Kramers–Brillouin (WKB) limit has long been invoked to explain the observed radial decrease of Alfvén wave amplitude in the solar wind (J. W. Belcher 1971; A. Barnes & J. V. Hollweg 1974; M. Heinemann & S. Olbert 1980; M. Velli 1993), underscoring the quasi-particle nature of Alfvén waves. To the best of our knowledge, the term *Alfvénon* was first used by Y. Song & R. L. Lysak (1994), who distinguished two types: the shear Alfvénon (shear Alfvén wave) and the compressional Alfvénon (fast wave). Subsequently, various studies have adopted this terminology to describe solitary Alfvén waves (see e.g. M. Akbari-Moghanjoughi 2011; K. Stasiewicz & J. Ekeberg 2008). Similarly, the term *Alfvén soliton* has also been used to refer to solitary Alfvén waves (see e.g. E. Mjølhus & J. Wyller 1986), and even interchangeably with Alfvénon (K. Stasiewicz 2006). It is therefore necessary to clarify our choice of nomenclature.

First, the term *Alfvén soliton* may be misleading. Solitons imply that colliding counter-propagating wave packets preserve their shape after interaction. How-

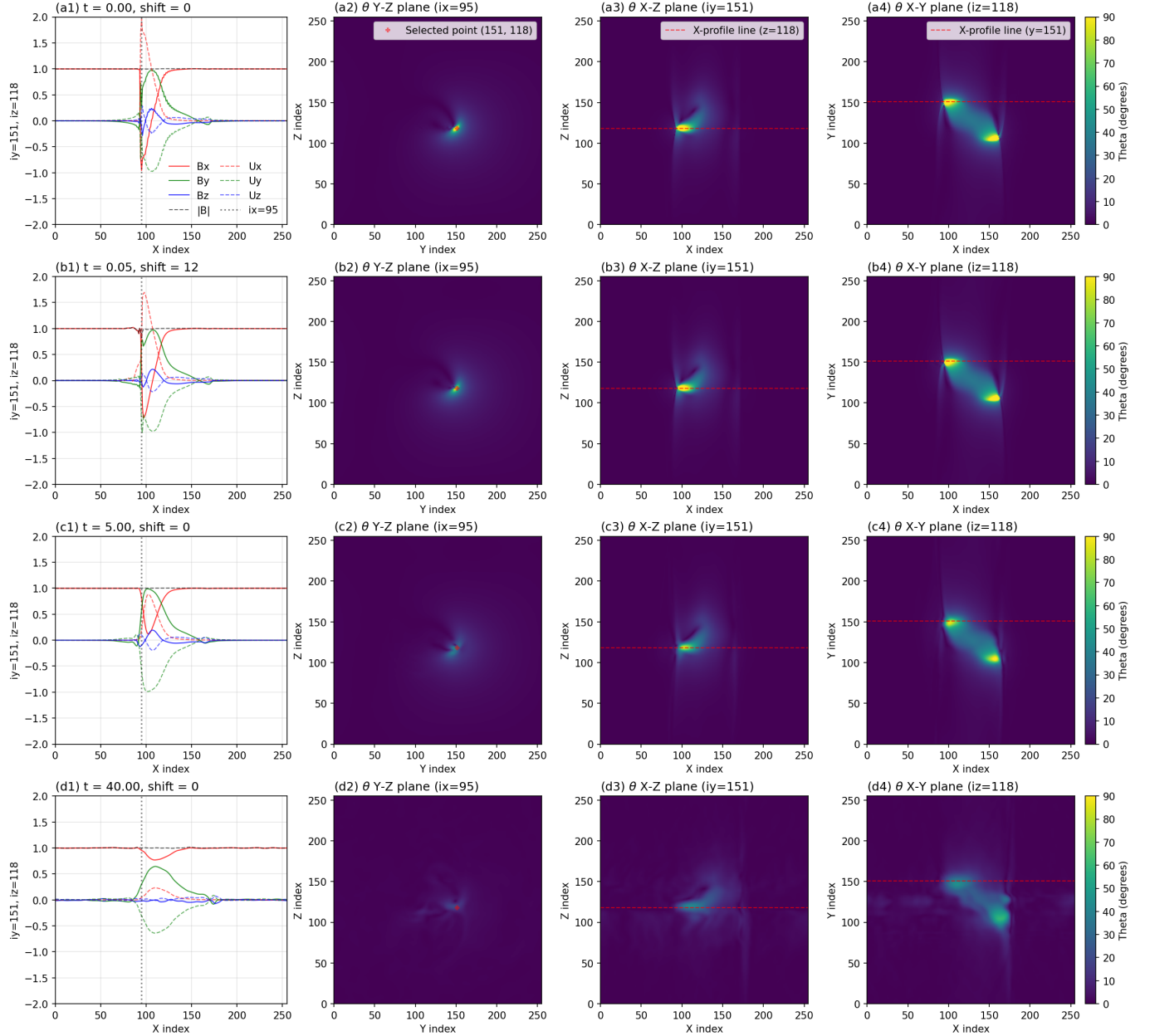


Figure 4. Spatial profiles and field-line angles at four times ($t = 0.00, 0.05, 5.00, 40.00$). *Column 1:* 1D cuts of $|B|$, B_x , B_y , B_z , u_x , u_y , u_z along the x -axis at $iy = 151$, $iz = 118$. *Columns 2–4:* 2D slices of $\theta = \cos^{-1}(B_x/|B|)$ at planes $ix = 95$, $iy = 151$, and $iz = 118$, respectively.

ever, counter-propagating Alfvén wave packets should undergo nonlinear interactions that deform the wave packets upon collision (see e.g. R. Kraichnan 1965; P. S. Iroshnikov 1964; M. Velli et al. 1992; B. D. G. Chandran & J. V. Hollweg 2009). Simulations using our model reveal that two counter-propagating solitary Alfvén wave packets undergo dramatic destruction upon collision, reminiscent of matter–antimatter annihilation. Details of this interaction will be presented in a forthcoming paper.

As demonstrated in Section 2, solitary Alfvén waves are perturbations of the magnetic field lines, analogous to shear Alfvén waves, and therefore naturally favor open field-line topology. As argued in Appendix A, any solitary solution with open field-line topology requires genuine three-dimensional coordinate dependence; otherwise, topologically closed regions inevitably arise. Previous “Alfvénon” models have been predominantly either 1D dependent (without constant $|B|$) or 2D/2.5D dependent (containing topologically closed regions). We further note that magnetosonic wave packets may not

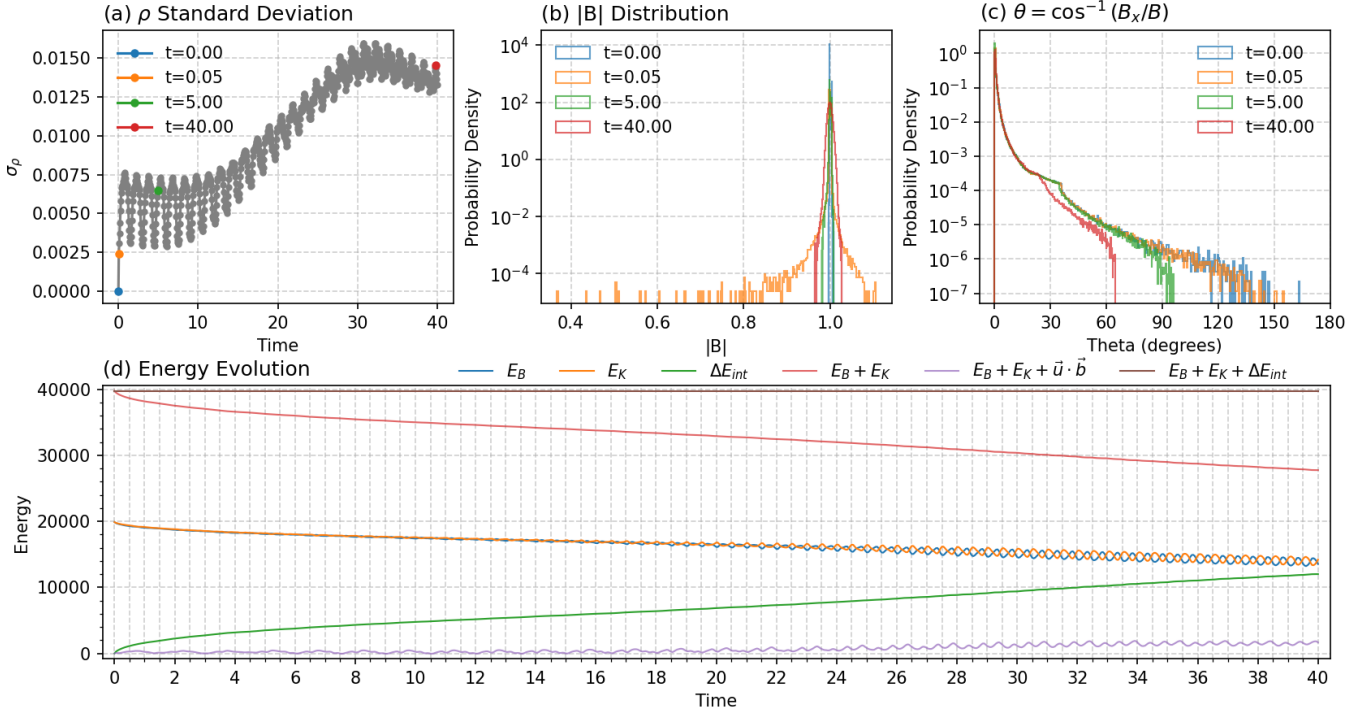


Figure 5. Time evolution. (a) Standard deviation of ρ versus time. Probability histograms at $t = 0.00, 0.05, 5.00$, and 40.00 for (b) density ρ and (c) angle $\theta = \cos^{-1}(B_x/|B|)$. (d) Magnetic, kinetic and Internal energy versus time.

merit the Alfvénon designation. Similar to pure sound waves, magnetosonic modes are self-resonant and naturally steepen into shocks that dissipate rapidly (Z. Huang et al. 2022). It is well established that in highly magnetized plasmas, the Alfvén mode is the only vehicle capable of transporting energy and information over large distances. The model constructed in this study is solitary with open field lines and exhibits remarkable stability in simulations, displaying quasi-particle characteristics that justify the nomenclature Alfvénon.

5.3. Conclusions

The open field-line geometry of the Alfvénon carries two intriguing implications. First, the wave’s stability likely arises from its distinctive three-dimensional pattern of twist and curvature, indicating coherence is geometric rather than topological. The convergent algorithm naturally selects specific twisting patterns that are physically feasible or favorable. Notably, the strong switchbacks in the model typically manifest as sharp rotational discontinuities, consistent with observations (see Fig. 1). Thus, the algorithm is not only numerically/geometrically interesting; it also reveals fundamental physical constraints. Second, the non-trivial twisting of the Alfvénon’s magnetic field lines makes it more “space-filling” than the unperturbed field. In a spherical expansion, the unperturbed B_r (and hence $|B|$) is expected to decline as R^{-2} due to magnetic-flux

conservation. However, recent studies show that in open coronal-hole regions, both B_r and $|B|$ decline systematically more slowly than R^{-2} (S. D. Bale et al. 2023; Z. Huang et al. 2024b). This space-filling property may therefore contribute to the observed deviation from the canonical flux-conservation scaling.

We also note that SPAWs—and thus Alfvénons—are exact solutions of relativistic MHD (A. Mallet & B. D. G. Chandran 2021). In strongly magnetized environments where the Alfvén speed approaches the speed of light, relativistic Alfvénons could transport energy far more efficiently than classical shear Alfvén waves via their ultra-relativistic jets. Recent studies have proposed Alfvén waves as viable drivers of fast radio bursts (FRBs) from magnetars (Y. Yuan et al. 2021, 2022; P. Kumar & Ž. Bošnjak 2020; K. Long & A. Pe’er 2025; A. Y. Chen et al. 2025). Investigating the behavior, stability, energy transport, and collision properties of relativistic Alfvénons is an exciting direction for future research.

To the best of our knowledge, this work represents the first numerical realization of a solitary three-dimensional spherically polarized Alfvén wave packet (Alfvénon), an exact nonlinear solution of the ideal MHD equations. Analogous to shear Alfvén waves, the Alfvénon exhibits nontrivial three-dimensional twisting of magnetic field lines. Its complex structure and remark-

able stability suggest that fundamental aspects of Alfvén wave physics remain incompletely understood, more than eight decades after its original conceptualization. Moreover, the ubiquity of solitary Alfvén waves in the highly magnetized solar corona suggests that such localized structures may constitute the dominant form of Alfvénic fluctuations in astrophysical environments. Our convergent algorithm therefore provides a foundation for future investigations of solitary Alfvén wave physics in various contexts.

The python implementation of convergent algorithm is publicly available at https://github.com/huangzesen/Helmholtz_algo_public.

ACKNOWLEDGMENTS

Z.H. thanks Benjamin Chandran, John. W. Belcher, Margaret G. Kivelson, Krishan Khurana, Yingdong Jia, and Robert Strangeway for stimulating discussions. Claude AI and ChatGPT have been used extensively in preparing this work. Specifically, the original idea of the algorithm was produced via interaction with Claude AI. This work is supported by NASA HTMS 80NSSC20K1275 and NASA AIAH 80NSSC25K0386. C.S. acknowledges supported from NSF SHINE 2229566 and NASA ECIP 80NSSC23K1064.

AUTHOR CONTRIBUTIONS

Z.H. conceived the idea, designed the study, conducted the MHD simulations, and wrote the manuscript. M.V. contributed to the conceptual framework and provided critical guidance throughout the study. C.S. provided technical support for the simulation code and contributed to the conceptual development. Y.D. contributed to the theoretical framework. All authors reviewed and revised the manuscript.

APPENDIX

A. 3D DEPENDENCE OF SIMPLY CONNECTED MAGNETIC SOLITARY SOLUTION

Let $\mathbf{V} : \mathbb{R}^3 \rightarrow \mathbb{R}^3$ be a vector field that approaches a constant value at spatial infinity:

$$\mathbf{V}(\mathbf{x}) \rightarrow \mathbf{V}_\infty \quad \text{as } \|\mathbf{x}\| \rightarrow \infty.$$

No assumptions are imposed on the divergence, curl, or magnitude of \mathbf{V} . Suppose that in some coordinate system (q_1, q_2, q_3) the field depends on only two variables:

$$\mathbf{V}(q_1, q_2, q_3) = \mathbf{V}(q_1, q_2).$$

CLAIM

A nontrivial isolated configuration of this type is only possible if the suppressed coordinate q_3 parametrizes a *compact loop* in physical space. If q_3 is unbounded, the only vector field satisfying the asymptotic condition is the trivial uniform field \mathbf{V}_∞ .

ARGUMENT

For each fixed (q_1, q_2) , the field remains constant as q_3 varies. Define the set

$$\Gamma_{(q_1, q_2)} = \{(q_1, q_2, q_3) : q_3 \in I\},$$

where I is the range of q_3 . All points in $\Gamma_{(q_1, q_2)}$ share the same field value $\mathbf{V}(q_1, q_2)$.

Case 1: q_3 unbounded. If q_3 ranges over an unbounded interval, then $\Gamma_{(q_1, q_2)}$ contains points with arbitrarily large Euclidean norm. Along this direction,

$$\mathbf{V}(q_1, q_2, q_3) = \mathbf{V}(q_1, q_2) \quad \text{for all } q_3.$$

If $\mathbf{V}(q_1, q_2) \neq \mathbf{V}_\infty$, then the field fails to approach \mathbf{V}_∞ along these unbounded lines, contradicting the assumed asymptotic behavior. Thus the condition at infinity forces

$$\mathbf{V}(q_1, q_2) = \mathbf{V}_\infty \quad \forall (q_1, q_2),$$

so \mathbf{V} is constant everywhere.

Case 2: q_3 compact. If q_3 parametrizes a topologically closed region (e.g. an angular coordinate), then each set $\Gamma_{(q_1, q_2)}$ is bounded. Nontrivial dependence on (q_1, q_2) does not produce directions along which the field propagates to infinity while remaining fixed. Therefore the field may coincide with \mathbf{V}_∞ outside a sufficiently large ball while retaining nontrivial structure in a compact region.

CONCLUSION

A vector field on \mathbb{R}^3 that becomes uniform at infinity and depends on only two coordinates can exhibit nontrivial localized structure only if the remaining coordinate is spatially bounded, forming topologically closed regions. If the unused coordinate is unbounded, the asymptotic condition forces the field to be identically equal to the far-field constant \mathbf{V}_∞ .

B. CONVERGENT ALGORITHM IMPLEMENTATION

B.1. Helmholtz-Hodge Decomposition in Fourier Space

The Helmholtz-Hodge decomposition:

$$\vec{F} = \nabla \varphi + \nabla \times \vec{A} = \vec{F}_\parallel + \vec{F}_\perp \tag{B1}$$

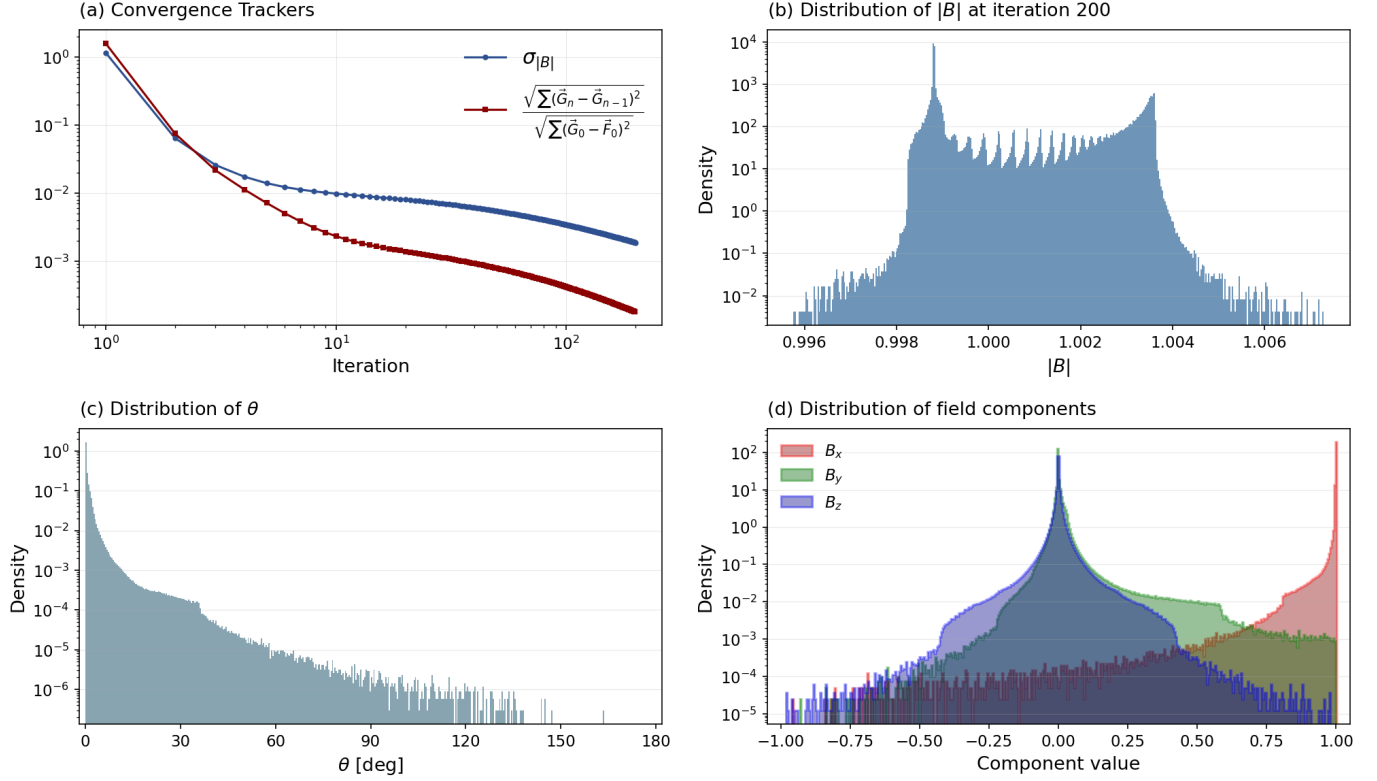


Figure 6. Convergence and statistical properties of the final Alfvén model. (a) Convergence trackers: standard deviation σ_B of $|\vec{G}_n|$ and normalized field difference $\Delta\vec{G}_n$ versus iteration number. Probability histograms at iteration 200 for: (b) magnetic field magnitude $|B|$, (c) field-line angle $\theta = \cos^{-1}(B_x/|B|)$, (d) magnetic field components B_x , B_y , and B_z .

is conducted in the Fourier space by solving the Poisson equation:

$$\widehat{\nabla \cdot \vec{F}} = i\vec{k} \cdot \widehat{\vec{F}} = \widehat{\Delta\varphi} = -k^2 \widehat{\varphi}. \quad (\text{B2})$$

and thus the potential field is obtained to be:

$$\widehat{\varphi} = -\frac{i\vec{k} \cdot \widehat{\vec{F}}}{k^2}, \quad (\text{B3})$$

where the zero- k singular point $\widehat{\varphi}(0)$ is set to be an arbitrary value. The solenoidal field can then be obtained:

$$\begin{aligned} \widehat{F}_\perp &= \widehat{\vec{F}} - \widehat{\nabla\varphi} = \widehat{\vec{F}} - \left[i\vec{k} \left(-\frac{i\vec{k} \cdot \widehat{\vec{F}}}{k^2} \right) \right] \\ &= \widehat{\vec{F}} - \vec{k} \left(\frac{\vec{k} \cdot \widehat{\vec{F}}}{k^2} \right). \end{aligned} \quad (\text{B4})$$

\widehat{F}_\perp can then be inverse-transformed into real space, which is denoted as \vec{G} . In practice, the values of $\widehat{\vec{F}}$ and \widehat{F}_\perp on the Nyquist planes are set to zero to avoid aliasing. Otherwise, significant divergence persists in \vec{G} for $|k| \geq k_{\text{Nyquist}}$.

B.2. Constructing Alfvén Model

We construct the model on a 256^3 grid with all spatial coordinates x , y , and z ranging from 0 to 1. The vector at each grid point is denoted $\vec{B}(x, y, z) = (B_x(x, y, z), B_y(x, y, z), B_z(x, y, z))$. The initial field \vec{F}_0 consists of a uniform background $\vec{B}_0 = (1, 0, 0)$ superposed with a large-amplitude circularly polarized Alfvén wave, modulated by a Gaussian envelope centered in the domain to produce spatial localization:

$$\vec{F}_0 = \vec{B}_0 + A \cdot [\cos(\phi)\hat{y} + \sin(\phi)\hat{z}] \cdot \exp\left[-\frac{\Delta r^2}{2\sigma^2}\right], \quad (\text{B5})$$

where $A = 100.0$, $\phi = 2\pi k_x x$, $k_x = 4$, $\Delta r = \sqrt{(x-0.5)^2 + (y-0.5)^2 + (z-0.5)^2}$, and $\sigma = 1/30$. Because of the Gaussian envelope, \vec{F}_0 is neither divergence-free nor of constant magnitude, making it a suitable input for the algorithm.

Convergence is monitored by tracking the standard deviation σ_B of $|\vec{G}_n|$ and the normalized vector field difference:

$$\Delta\vec{G}_n = \frac{\sqrt{\sum(\vec{G}_n - \vec{G}_{n-1})^2}}{\sqrt{\sum(\vec{G}_0 - \vec{F}_0)^2}} \quad (\text{B6})$$

at each step, as shown in Figure 6(a). After 200 iterations, σ_B in \vec{G}_{200} becomes negligible relative to the spreads in B_x , B_y , and B_z (Fig. 6b–d), while $\Delta\vec{G}_n$ indicates convergence of the field. Notably, a substantial fraction of grid points exhibit $\theta > 90^\circ$ (where $\theta = \cos^{-1}(B_x/|\vec{B}|)$), confirming the presence of field reversals characteristic of magnetic switchbacks. We therefore adopt \vec{G}_{200} as a candidate for the Alfvénon and denote it simply as \vec{G}_A .

C. DIAGNOSTICS OF MHD SIMULATIONS

Magnetic Energy E_B :

$$E_B = \sum_{ijk} \frac{1}{2} |\vec{B} - \vec{B}_0|^2 \quad (\text{C7})$$

where $\vec{B}_0 = (1, 0, 0)$ is the unperturbed background field.

Kinetic Energy E_K :

$$E_K = \sum_{ijk} \frac{1}{2} \rho |\vec{u}|^2 \quad (\text{C8})$$

Internal Energy Variation ΔE_{int} : The internal energy density is defined as

$$E_{\text{int}} = \sum_{ijk} \frac{p}{\gamma - 1}, \quad (\text{C9})$$

where $\gamma = 1.1$. To track deviations from the initial equilibrium, we compute

$$\Delta E_{\text{int}} = E_{\text{int}}(t) - E_{\text{int}}(t = 0). \quad (\text{C10})$$

Alfvénic Energy Residual: For a pure forward-propagating Alfvén wave, the quantity

$$E_{\text{res}} = E_K + E_B + \sum_{ijk} \vec{u} \cdot \vec{b} \quad (\text{C11})$$

vanishes identically, where $\vec{b} = \vec{B}/\sqrt{\mu_0\rho}$. Nonzero E_{res} therefore indicates the presence of non-Alfvénic energy (e.g., magnetosonic modes or turbulent cascade). We use this diagnostic as an indicator of deviations from the pure Alfvénic state.

D. FIELD LINE TOPOLOGY

A Runge-Kutta method is employed to trace the field lines. Given the magnetic grid $\{B_x, B_y, B_z\}$ on a periodic box of size \mathbf{L} , each component is trilinearly interpolated to an arbitrary point \mathbf{x} :

$$\mathbf{B}(\mathbf{x}) = (B_x(\mathbf{x}), B_y(\mathbf{x}), B_z(\mathbf{x})),$$

with indices wrapped periodically before interpolation. The local direction field is then

$$\hat{\mathbf{b}}(\mathbf{x}) = \begin{cases} \frac{\mathbf{B}(\mathbf{x})}{\|\mathbf{B}(\mathbf{x})\|}, & \|\mathbf{B}(\mathbf{x})\| > 10^{-12}, \\ \mathbf{0}, & \text{otherwise.} \end{cases}$$

Starting from a seed \mathbf{x}_0 , Runge–Kutta 4 (step size h) advances along this interpolated, unit-magnitude field:

$$\begin{aligned} \mathbf{k}_1 &= \hat{\mathbf{b}}(\mathbf{x}_n), \\ \mathbf{k}_2 &= \hat{\mathbf{b}}(\mathbf{x}_n + \tfrac{1}{2}h\mathbf{k}_1), \\ \mathbf{k}_3 &= \hat{\mathbf{b}}(\mathbf{x}_n + \tfrac{1}{2}h\mathbf{k}_2), \\ \mathbf{k}_4 &= \hat{\mathbf{b}}(\mathbf{x}_n + h\mathbf{k}_3), \\ \mathbf{x}_{n+1} &= \text{mod}(\mathbf{x}_n + \tfrac{h}{6}(\mathbf{k}_1 + 2\mathbf{k}_2 + 2\mathbf{k}_3 + \mathbf{k}_4), \mathbf{L}). \end{aligned}$$

Each step samples the trilinearly interpolated $\hat{\mathbf{b}}$ at the intermediate RK4 positions and wraps the result back into the periodic domain, producing the traced field line forward and/or backward from the seed.

To determine whether topologically closed regions exist in \vec{G}_A , we forward-track field lines from every point on the $x = 0$ ($\text{ix} = 0$) surface and backward-track from every point on the $x = 1.0$ ($\text{ix} = 255$) surface. Points traversed by any field line are marked as visited. This bidirectional tracking covers 16,600,404 out of 16,777,216 grid points (98.95%), with the remaining unvisited points shown in the left panel of Figure 7.

Among the 176,812 unvisited points, the majority (175,452, 99.23%) lie near the y and z boundary surfaces (red), which is expected given the negligible field-line curvature in those regions. The remaining 1,360 points (0.77%) appear as blue scatter in both panels. Notably, these points are sparsely distributed rather than clustered, indicating they do not correspond to closed magnetic field regions. Their exclusion stems primarily from their location in zones of particularly strong field-line curvature, where finite grid resolution limits the precision of field-line tracking. Indeed, as visualized in Fig. 3, these points coincide with the strongly curved regions.

To confirm that these “untouched islands” do not form closed field-line loops, we perform both forward and backward tracking from each of these points. The results are shown in right panel of Figure 7. All field lines passing through these points extend naturally to the $x = 0$ and $x = 1$ surfaces, consistent with the open topology of the unperturbed background field. Moreover, the field lines exhibit remarkable complexity within the perturbed region of the *Alfvén*on. Readers are encouraged to explore the interactive versions of these figures provided in the supplementary materials.

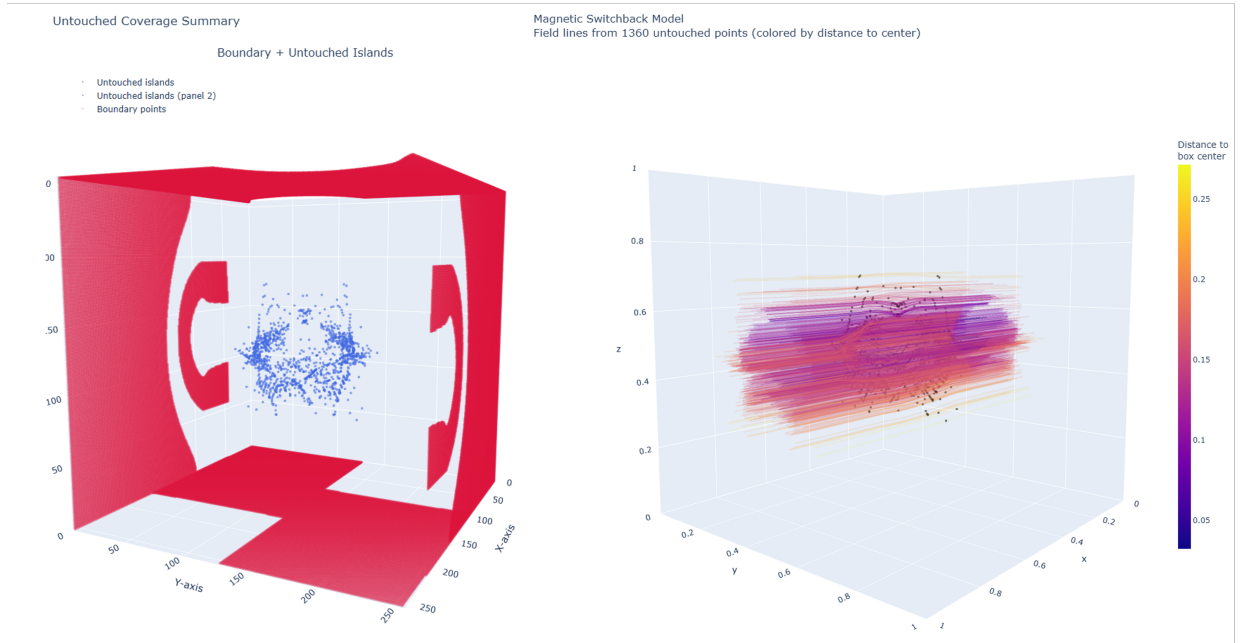


Figure 7. *Left:* Distribution of untouched points. *Right:* Field lines passing the “untouched islands”.

REFERENCES

- Akbari-Moghanjoughi, M. 2011, *Physics of Plasmas*, 18, 042107, doi: [10.1063/1.3581075](https://doi.org/10.1063/1.3581075)
- Alfvén, H. 1942, *Nature*, 150, 405, doi: [10.1038/150405d0](https://doi.org/10.1038/150405d0)
- Bale, S. D., Goetz, K., Harvey, P. R., et al. 2016, *fr*, 204, 49, doi: [10.1007/s11214-016-0244-5](https://doi.org/10.1007/s11214-016-0244-5)
- Bale, S. D., Badman, S. T., Bonnell, J. W., et al. 2019, *Nature*, 576, 237, doi: [10.1038/s41586-019-1818-7](https://doi.org/10.1038/s41586-019-1818-7)
- Bale, S. D., Drake, J. F., McManus, M. D., et al. 2023, *Nature*, 618, 252, doi: [10.1038/s41586-023-05955-3](https://doi.org/10.1038/s41586-023-05955-3)
- Barnes, A. 1981, *Journal of Geophysical Research: Space Physics*, 86, 7498, doi: [10.1029/JA086iA09p07498](https://doi.org/10.1029/JA086iA09p07498)
- Barnes, A., & Hollweg, J. V. 1974, *Journal of Geophysical Research*, 79, 2302, doi: [10.1029/JA079i016p02302](https://doi.org/10.1029/JA079i016p02302)
- Belcher, J. W. 1971, *Astrophysical Journal*, vol. 168, p.509, doi: [10.1086/151105](https://doi.org/10.1086/151105)
- Belcher, J. W., & Davis, L. 1971, *Journal of Geophysical Research*, 76, 3534, doi: [10.1029/JA076i016p03534](https://doi.org/10.1029/JA076i016p03534)
- Chandran, B. D. G. 2018, *Journal of Plasma Physics*, 84, 905840106, doi: [10.1017/S0022377818000016](https://doi.org/10.1017/S0022377818000016)
- Chandran, B. D. G., & Hollweg, J. V. 2009, *The Astrophysical Journal*, 707, 1659, doi: [10.1088/0004-637X/707/2/1659](https://doi.org/10.1088/0004-637X/707/2/1659)
- Chen, A. Y., Yuan, Y., & Bernardi, D. 2025, *The Astrophysical Journal*, 987, 42, doi: [10.3847/1538-4357/adda3b](https://doi.org/10.3847/1538-4357/adda3b)
- Coleman, Paul J., J. 1968, *apj*, 153, 371, doi: [10.1086/149674](https://doi.org/10.1086/149674)
- Derby, Jr., N. F. 1978, *The Astrophysical Journal*, 224, 1013, doi: [10.1086/156451](https://doi.org/10.1086/156451)
- Fox, N. J., Velli, M. C., Bale, S. D., et al. 2016, *Space Science Reviews*, 204, 7, doi: [10.1007/s11214-015-0211-6](https://doi.org/10.1007/s11214-015-0211-6)
- Gekelman, W., Vincena, S., Leneman, D., & Maggs, J. 1997, *Journal of Geophysical Research: Space Physics*, 102, 7225, doi: [10.1029/96JA03683](https://doi.org/10.1029/96JA03683)
- Goldstein, M. L., Klimas, A. J., & Barish, F. D. 1974, On the theory of large amplitude Alfvén waves, <https://ntrs.nasa.gov/citations/19740014712>
- Gosling, J. T., McComas, D. J., Roberts, D. A., & Skoug, R. M. 2009, *The Astrophysical Journal*, 695, L213, doi: [10.1088/0004-637X/695/2/L213](https://doi.org/10.1088/0004-637X/695/2/L213)
- Heinemann, M., & Olbert, S. 1980, *Journal of Geophysical Research: Space Physics*, 85, 1311, doi: [10.1029/JA085iA03p01311](https://doi.org/10.1029/JA085iA03p01311)
- Huang, Z., Shi, C., Sioulas, N., & Velli, M. 2022, *The Astrophysical Journal*, 935, 60, doi: [10.3847/1538-4357/ac74c5](https://doi.org/10.3847/1538-4357/ac74c5)
- Huang, Z., Velli, M., Shi, C., et al. 2024a, *The Astrophysical Journal Letters*, 977, L12, doi: [10.3847/2041-8213/ad9271](https://doi.org/10.3847/2041-8213/ad9271)
- Huang, Z., Shi, C., Velli, M., et al. 2024b, *The Astrophysical Journal Letters*, 973, L26, doi: [10.3847/2041-8213/ad72f1](https://doi.org/10.3847/2041-8213/ad72f1)
- Iroshnikov, P. S. 1964, *\sovast*, 7, 566
- Kasper, J. C., Abiad, R., Austin, G., et al. 2016, *fr*, 204, 131, doi: [10.1007/s11214-015-0206-3](https://doi.org/10.1007/s11214-015-0206-3)
- Kasper, J. C., Bale, S. D., Belcher, J. W., et al. 2019, *Nature*, 576, 228
- Kasper, J. C., Klein, K. G., Lichko, E., et al. 2021, *Physical Review Letters*, 127, 255101, doi: [10.1103/PhysRevLett.127.255101](https://doi.org/10.1103/PhysRevLett.127.255101)
- Kraichnan, R. 1965, doi: [10.1063/1.1761412](https://doi.org/10.1063/1.1761412)
- Kruparova, O., Krupar, V., Szabo, A., Pulupa, M., & Bale, S. D. 2023, *The Astrophysical Journal*, 957, 13, doi: [10.3847/1538-4357/acf572](https://doi.org/10.3847/1538-4357/acf572)
- Kumar, P., & Bošnjak, Ž. 2020, *Monthly Notices of the Royal Astronomical Society*, 494, 2385, doi: [10.1093/mnras/staa774](https://doi.org/10.1093/mnras/staa774)
- Long, K., & Pe'er, A. 2025, Fast Radio Bursts from non-resonant Alfvén waves and synchrotron maser emission in the magnetar wind, *arXiv*, doi: [10.48550/arXiv.2508.05840](https://doi.org/10.48550/arXiv.2508.05840)
- Mallet, A., & Chandran, B. D. G. 2021, *Journal of Plasma Physics*, 87, 175870601, doi: [10.1017/S0022377821000970](https://doi.org/10.1017/S0022377821000970)
- McKee, C. F., & Zweibel, E. G. 1995, *The Astrophysical Journal*, 440, 686, doi: [10.1086/175306](https://doi.org/10.1086/175306)
- Mjølhus, E., & Wyller, J. 1986, *Physica Scripta*, 33, 442, doi: [10.1088/0031-8949/33/5/011](https://doi.org/10.1088/0031-8949/33/5/011)
- Raouafi, N. E., Matteini, L., Squire, J., et al. 2023, *Space Science Reviews*, 219, 8, doi: [10.1007/s11214-023-00952-4](https://doi.org/10.1007/s11214-023-00952-4)
- Shi, C., Velli, M., Bale, S. D., et al. 2022, *Physics of Plasmas*, 29, 122901, doi: [10.1063/5.0124703](https://doi.org/10.1063/5.0124703)
- Shi, C., Tenerani, A., Rappazzo, A. F., & Velli, M. 2024a, *Frontiers in Astronomy and Space Sciences*, 11, doi: [10.3389/fspas.2024.1412905](https://doi.org/10.3389/fspas.2024.1412905)
- Shi, C., Velli, M., Toth, G., et al. 2024b, *The Astrophysical Journal Letters*, 964, L28, doi: [10.3847/2041-8213/ad335a](https://doi.org/10.3847/2041-8213/ad335a)
- Shoda, M., Chandran, B. D. G., & Cranmer, S. R. 2021, *The Astrophysical Journal*, 915, 52, doi: [10.3847/1538-4357/abfdbc](https://doi.org/10.3847/1538-4357/abfdbc)
- Song, Y., & Lysak, R. L. 1994, *Geophysical Research Letters*, 21, 1755, doi: [10.1029/94GL01327](https://doi.org/10.1029/94GL01327)
- Squire, J., & Mallet, A. 2022, *Journal of Plasma Physics*, 88, 175880503, doi: [10.1017/S0022377822000848](https://doi.org/10.1017/S0022377822000848)
- Stasiewicz, K. 2006, *Physical Review Letters*, 96, 175003, doi: [10.1103/PhysRevLett.96.175003](https://doi.org/10.1103/PhysRevLett.96.175003)
- Stasiewicz, K., & Ekeberg, J. 2008, *The Astrophysical Journal*, 680, L153, doi: [10.1086/589878](https://doi.org/10.1086/589878)

- Tenerani, A., Velli, M., Matteini, L., et al. 2020, The Astrophysical Journal Supplement Series, 246, 32, doi: [10.3847/1538-4365/ab53e1](https://doi.org/10.3847/1538-4365/ab53e1)
- Unti, T. W. J., & Neugebauer, M. 1968, The Physics of Fluids, 11, 563, doi: [10.1063/1.1691953](https://doi.org/10.1063/1.1691953)
- Velli, M. 1993, Astronomy and Astrophysics, 270, 304. <https://ui.adsabs.harvard.edu/abs/1993A&A...270..304V>
- Velli, M., Grappin, R., & Mangeney, A. 1992, AIP Conference Proceedings, 267, 154, doi: [10.1063/1.42861](https://doi.org/10.1063/1.42861)
- Yuan, Y., Beloborodov, A. M., Chen, A. Y., et al. 2022, The Astrophysical Journal, 933, 174, doi: [10.3847/1538-4357/ac7529](https://doi.org/10.3847/1538-4357/ac7529)
- Yuan, Y., Levin, Y., Bransgrove, A., & Philippov, A. 2021, The Astrophysical Journal, 908, 176, doi: [10.3847/1538-4357/abd405](https://doi.org/10.3847/1538-4357/abd405)